

## GPS meteorology: An investigation of ocean-based precipitable water estimates

John Kealy,<sup>1</sup> James Foster,<sup>1</sup> and Steven Businger<sup>1</sup>

Received 29 December 2011; revised 13 July 2012; accepted 16 July 2012; published 8 September 2012.

[1] A study of ship-based precipitable water (PW) estimation using the global positioning system (GPS) is presented for a field experiment in the coastal waters of Hawai'i. GPS precipitable water estimates, with a temporal resolution of 30 min, are shown to agree with radiosonde observations with an RMS error of 2.16 mm. The GPS PW time series is shown to possess significant value in identifying atmospheric features at both synoptic and mesoscale resolution throughout the experiment. Examples include influences from an upper level low-pressure system, shear lines, island blocking, and zones of low level convergence. Given PW's high spatial and temporal variability and the fact that it is not dynamically tied to other variables such as pressure or temperature, future PW estimates from ships could provide an important constraint for numerical weather prediction (NWP) models over ocean regions.

**Citation:** Kealy, J., J. Foster, and S. Businger (2012), GPS meteorology: An investigation of ocean-based precipitable water estimates, *J. Geophys. Res.*, 117, D17303, doi:10.1029/2011JD017422.

### 1. Introduction

[2] The role of water vapor in the atmosphere is paramount to understanding and predicting weather systems and atmospheric processes, from planetary to convective scales. When the vapor condenses in clouds, the latent heat released fuels convection and cyclogenesis, making knowledge of its distribution of paramount importance to weather analysis and forecasting. With the inception of space-based geodesy, a largely unanticipated use of the global positioning system (GPS) to measure total column precipitable water vapor (PW) became available to meteorologists [Bevis *et al.*, 1992]. This method of deriving PW has been investigated extensively [Bevis *et al.*, 1994; Rocken *et al.*, 1993, 1995; Duan *et al.*, 1996; Tregoning *et al.*, 1998] and been proven to be as accurate as, and in many cases more accurate than, conventional methods of observing PW such as radiometers, radiosondes and satellites [Businger *et al.*, 1996]. As a result, there now exists an extensive network of land based GPS receivers that provide low cost, high-accuracy estimates of atmospheric PW globally.

[3] Because PW is spatially highly variable and not dynamically tied to other variables such as pressure or temperature, PW provides a powerful constraint for numerical weather prediction (NWP) models. GPS PW has been successfully assimilated into NWP models [e.g., Kuo *et al.*, 1993; Rocken *et al.*, 1997; Gutman *et al.*, 2004], and more

recently been made available for near real time model initialization with the aid of techniques like the sliding window analysis [Rocken *et al.*, 1997; Foster *et al.*, 2005; Smith *et al.*, 2007]. GPS PW estimation has also been useful in observational studies of weather and climate [e.g., Gradinarsky *et al.*, 2002; Foster *et al.*, 2003].

[4] One significant limitation of GPS PW networks thus far has been the fact that receivers are only located on land. Ocean PW measurement is largely reliant on satellite instruments, such as the near infrared water-vapor channel of the Moderate-Resolution Imaging Spectroradiometer (MODIS). The drawback of the method by which MODIS determines PW is that reflected solar radiation from the ocean surface is required, making the measurements unavailable in cloudy areas and at night [Gao and Kaufman, 2003]. This limits MODIS PW observations to 25% globally [Li *et al.*, 2003], therefore, an alternative method of ocean PW estimation is needed. Microwave instruments, such as the Special Sensor Microwave/Imager, Special Sensor Microwave Imager Sounder, and the Advanced Microwave Sounding Unit, provide reasonably accurate (~2.5–3+ mm [e.g., Sohn and Smith, 2003]) maps of ocean PW values but, as they are sun-synchronous, they give only 6-hourly snapshots, with the satellites providing little information on sub-daily changes and diurnal variations, and have a relatively low spatial resolution.

[5] Oceanic PW estimation using GPS has shown promise in recent years. Chadwell and Bock [2001] first investigated the technique using a moored buoy fitted with a GPS receiver off the California coast, and obtained GPS PW estimates that agreed well with nearby land-based estimates and radiosondes. Rocken *et al.* [2005] extended this work to PW estimation using a GPS receiver aboard a cruise ship in the open ocean. Their results show that, despite the inherent difficulty in taking measurements aboard a platform that

<sup>1</sup>Department of Meteorology, University of Hawai'i at Mānoa, Honolulu, Hawai'i, USA.

Corresponding author: S. Businger, Department of Meteorology, University of Hawai'i at Mānoa, 2525 Correa Rd., Honolulu, HI 96822, USA. (businger@hawaii.edu)

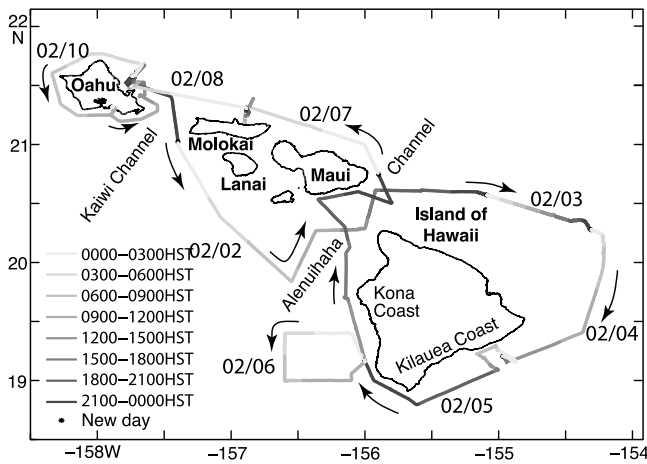


**Figure 1.** *Kilo Moana* track around the Hawaiian Islands. Times, dates, reference GPS sites, and selected locations are provided along the track.

moves both horizontally and vertically with ocean waves, accurate GPS PW estimates from ocean-based receivers can be obtained. With the large number of ships in transit across the oceans and seas at any given time, there is potential for a wide network of oceanic PW observations [e.g., *Foster et al.*, 2012], and the assimilation of ship-based PW measurements would likely improve the accuracy of NWP.

[6] This study includes a comprehensive meteorological analysis to demonstrate the potential of ship-based GPS meteorology to resolve synoptic and mesoscale features and processes present during a field experiment around the Hawaiian Islands. Hawai'i, with its subtropical climate, is an ideal location to test the technique, being influenced by synoptic-scale features such as cold fronts and subtropical cyclones [*Morrison and Businger*, 2001], and mesoscale features induced by the interaction of the winds with the island's topography [*Smith and Grubišić*, 1993].

[7] The field experiment took place aboard a research vessel in Hawai'i's coastal waters, encountering both synoptic and island-scale weather features in dynamically unstable conditions. As well as validating the GPS PW data throughout the cruise using radiosondes, the PW time series is also analyzed in terms of its ability to resolve the signatures of these weather features. Independent meteorological data sets are employed to create analyses of the atmospheric state during the field experiment, and a discussion of how the GPS PW estimates relate to this external data set is provided.

## 2. Data and Methods

### 2.1. GPS Data and Processing

[8] The *R/V Kilo Moana* (KM) is equipped with twin Trimble BD950 geodetic GPS receivers and Trimble zephyr antennas as part of its navigation systems. Raw 1 Hz data from the GPS boards were recorded for the entire period of the 2011 cruise KM1103, starting at 16:57 day 032 UTC until 00:41 day 042 UTC (Figure 1). The two data sets were processed independently using the TRACK kinematic module of the GAMIT/GLOBK GPS processing software [*Herring*, 2006]. Four GPS stations were used as reference

sites, with their positions held fixed: POST (21.2973 N, 157.8164 W), at the University of Hawai'i at Mānoa, O'ahu; MAUI (20.7067 N, 156.2570 W), on the summit of Haleakala, Maui; MKEA (19.8014 N, 155.4563 W), near the summit of Mauna Kea, Hawai'i; and MLES (19.4643 N, 155.5525 W) located near the summit of Mauna Loa, Hawai'i.

[9] Multipath was partially mitigated by using custom static antenna phase variation maps for each reference site's antenna. Initial coordinates for the ship's antennas were estimated iteratively, with position constraints progressively tightened down to 1 m. A sliding window approach [*Foster et al.*, 2005] was then used, with four hours of data selected for processing, and the data window stepped forward two hours at a time.

[10] For each window, positions estimated from the previous window were provided as prior coordinates for the ship's GPS antennas with a 1-m constraint applied. Accurate and suitably constrained initial coordinates were found to significantly speed up the processing and improve its robustness. Precise IGS orbits were used, and all standard earth tides, and earth orientation parameters applied.

[11] The TRACK module estimates a tropospheric delay (zenith neutral delay, ZND) parameter for each observation epoch, with estimates treated as a constrained random walk, with 0.2 mm/sec error allowed (=12 mm/hr) for this project. The accuracy of the ZND estimates from TRACK is high for the relative delay between the reference and roving sites, but weak for absolute values [*Duan et al.*, 1996]. To address this, we set constant delay values for each of the four reference sites and derive independent time series of accurate relative delays between them and the ship. We then used the robust estimates of absolute delay for the reference sites, generated from static daily processing of a network of sites including the four reference sites from this study as well as many other sites distributed throughout the Pacific basin, to leverage the relative delays for the ship and produce equivalent absolute ZND time series. Shipboard measurements of the pressure and temperature were then used to transform the ZND time series into PW using a mapping function derived from NWS radiosonde profiles from Kaua'i and the Island of Hawai'i to convert surface temperature into mean weighted temperature [*Duan et al.*, 1996].

### 2.2. The GPS PW Time Series

[12] Half-hour averages for the mean of all the time series were calculated for each of the ship's GPS systems. This mean time series was formed in order to further reduce the impact of multipath artifacts introduced by reflecting surfaces around each of the antennas. The half-hour averaging was adopted because the higher-frequency variations in the ZND time series are expected to be largely dominated by noise in the data and residual multipath artifacts rather than actual changes in tropospheric refraction. The final GPS time series was obtained by averaging across the two antennas.

[13] The GPS time series represents estimates of PW for the KM cruise (Figure 2). This track was ideal for this study because of the variety of weather the ship encountered, including upwind island effects like orographic blocking, downwind effects like convergence zones, and channel effects like gap flows as well as exposure to larger scale weather patterns.

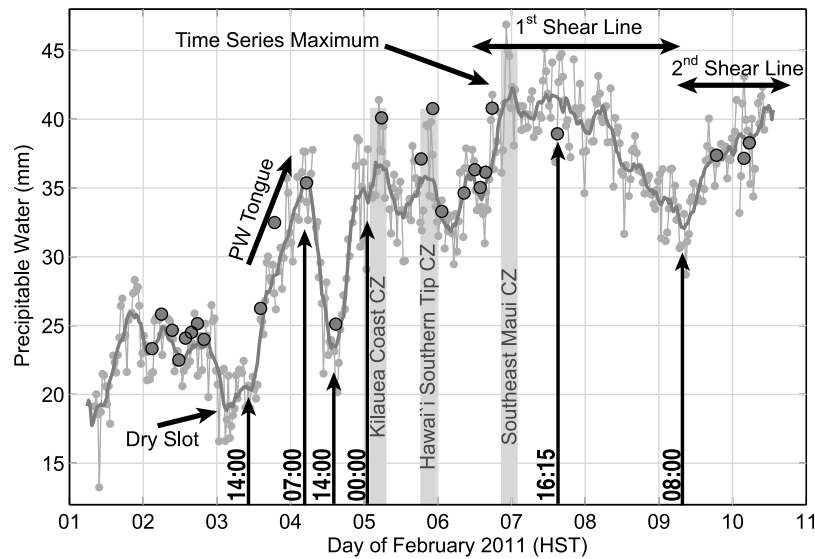


**Figure 2.** Time series of GPS PW estimates for the cruise (light gray) with a low-pass smoothing filter overlaid (dark gray). Radiosonde launches shown by black-edged circles. Important epochs and features are highlighted. Times shown in bold are referred to in the text.

[14] To validate their accuracy, the GPS PW estimates are compared to the PW observations from 26 Lockheed Martin LMG6 radiosondes launched during the cruise (Figure 3). We compare the GPS derived PW estimates at 30 min after the radiosonde launch time to match land-based comparisons, where the balloons are launched 30 min before the nominal observation time. This is also approximately the time taken for the balloon to rise through the moist lower troposphere. A correction of 0.23 mm of PW has been added to the GPS estimates to correct for the  $\sim 15$  m vertical offset between the GPS antennas and the deck from which the radiosonde were launched. The first balloon of the 26 launched reached only 1500 m and so was excluded from the comparisons. The best fit regression line has a slope of 0.97 and there is a mean offset of 1.2 mm between the GPS and radiosonde estimates with the radiosondes detecting more moisture. The  $r^2$  value is found to be 0.93, implying excellent agreement between the data sets, and the RMS difference for the PW is found to be 2.16 mm. This can be compared to the land-based RMS value of 1.76 mm found by *Motell et al.* [2002]. It should be noted that this difference will include errors in the radiosonde observations (estimated as 4% PW for plotting in Figure 3 [e.g., *Miloshevich et al.*, 2006], with GPS errors estimated as 1 mm PW), and also that the radiosonde observes a specific profile while the GPS estimate is based on a volume average. It is also clear from Figure 2 that many of the radiosonde PW values with the largest discrepancies from the GPS PW are at times when the GPS time series indicates strong PW gradients. Other considerations on the origin of error are that the KM is a relatively small cruise ship and the atmospheric and ocean conditions were more unstable than for the case of *Rocken et al.* [2005].

[15] High frequency variability of the order of 2–3 mm per 30-min interval is present in the time series between each data point (Figure 2). This may be partially a result of rapid variations in the depth of the mixed layer, where moisture

levels are highest. Observations of these rapid variations in the mixed layer depth have been inferred from lidar measurements of the coastal marine boundary layer over O‘ahu [*Porter et al.*, 2003]. They found that the mixed layer depth exhibited jumps of up to 1000 m over only a few tens of minutes. To test the magnitude of a potential contribution by this effect, the mixed layer depth in the sounding provided by radiosonde No. 9 was stretched by extending the top of the layer of constant potential temperature and specific humidity from the original 500 m up to 1000 m. This

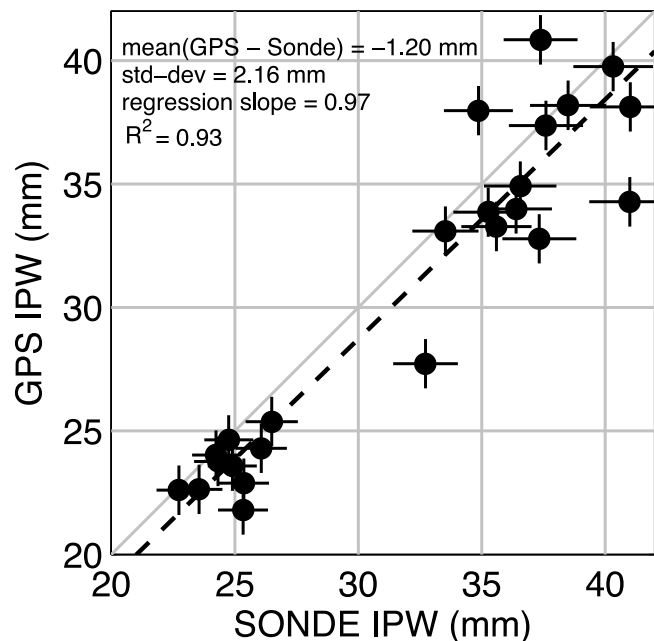


**Figure 3.** GPS PW plotted against Radiosonde PW. The mean difference is 1.2 mm (GPS PW drier), standard deviation = 2.16 mm and regression slope = 0.97. The  $r^2$  value is 0.93, implying good agreement.

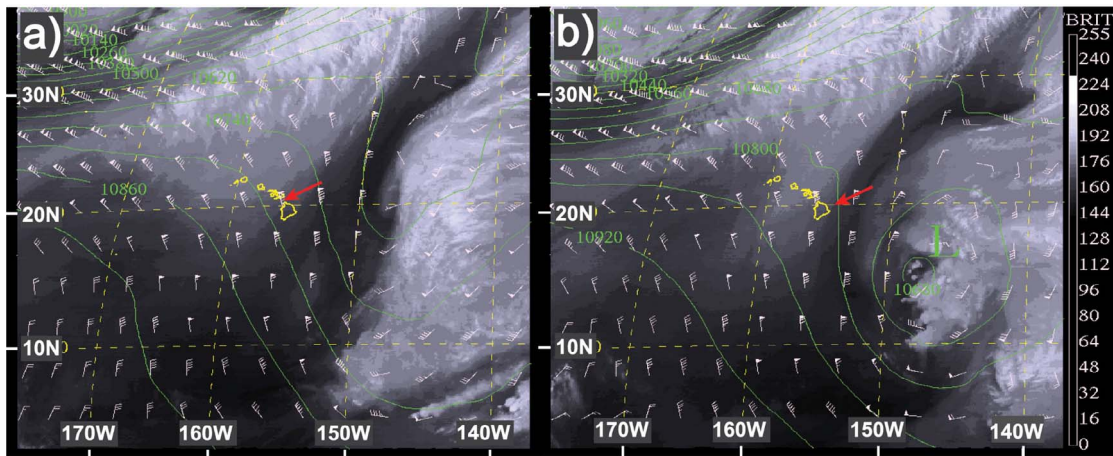


**Figure 4.** GOES WV images with Global Forecast Model (GFS) 250 mb height and wind analysis overlays for (a) 1400 HST on 2 February and (b) 1100 HST 3 February. KM indicates the positions of the *Kilo Moana*.

increased the PW from 24.3 mm to 25.5 mm., suggesting that at least some of the rapid variability we observed may be explained by this effect. We also note that several radiosonde measurements (Figure 2) appear to capture these PW spikes, corroborating the conclusion that we are measuring real changes, although some portion of the variability may be attributable to noise induced by the movement of the ship, and/or errors due to any remaining multipath signals.

[16] In order to further reduce noise and clearly identify meteorological signals in the time series, a low-pass, moving average smoothing filter is applied to the data with filter coefficients equal to the reciprocal of the span (Figure 2). A span of five hours was chosen in order to best smooth the data with respect to the amplitude of the noise, while maximizing the preservation of any meteorological signals. These signals arise because of changing weather conditions, which affect PW variability.

### 2.3. Meteorological Data

[17] External meteorological data are employed to validate the GPS PW estimates against the timing and positioning of weather features present during the field experiment, with respect to the ship's location. This external data comes from: 1) NOAA Doppler Radar stations PHKI (island of Kaua'i), PHMO (island of Moloka'i) and PHWA (island of Hawai'i); 2) 26 upper-air soundings from radiosondes launched over the course of the field experiment from the KM; 3) measurements of wind speed and direction, temperature, pressure, and precipitation collected by meteorological instruments aboard the vessel; 4) GOES-WEST water vapor (WV), infrared (IR), and visible (VIS) channels for the North Pacific Islands domain; and 5) PW, relative humidity, wind, and temperature analyses from the Local Analysis and Prediction System (LAPS). LAPS is a meteorological data assimilation tool that employs a suite of observations (meteorological networks, radiosondes, satellite, radar, aircraft, etc.) using a first guess from the weather research and forecasting model (WRF) to produce a three-dimensional, high resolution analysis of the atmosphere. A description of LAPS is provided by *Cherubini et al.* [2006], with a validation of selected variables by *Hiemstra et al.*

[2006]. Hawaiian Standard Time (HST) is used here because of the diurnally based flow regimes [*Chen and Nash*, 1994].

## 3. Results

### 3.1. Synoptic Situation

[18] The two main synoptic scale features present during the field experiment are an upper-level low pressure system to the east of the Hawaiian Islands, and a cold front to the northwest. The temperature gradient of the cold front dissipates before coming within 300 miles of Kaua'i, leaving a shear line that brings moisture to the islands.

[19] On 2 February, an upper-level low traveled toward Hawai'i from the northeastern Pacific, after becoming cut off from the midlatitude westerlies [*Simpson*, 1952; *Morrison and Businger*, 2001; *Caruso and Businger*, 2006]. The first, or incipient stage of the upper low is apparent at 1400 HST on 2 February (Figure 4a) where troughing in the 250 mb pressure level is accompanied by a jet streak, and associated dry slot, to the east of the islands [*Morrison and Businger*, 2001]. WV imagery shows this dry slot maintaining its position on the eastern edge of the islands throughout 3 February (Figure 4b) at the 350–400 mb level in the radiosonde sounding (Figure 5a). A drop of  $\sim 4$  mm occurs in GPS PW between 0000 HST and 1200 HST on 3 February, which can be attributed to the reduction in mid and upper-level moisture associated with this dry slot (Figure 2).

[20] By 1100 HST on 3 February, the cut-off low is clearly established at 250 mb (Figure 4b), with a cold-core observed in the LAPS 600 mb temperature analysis (not shown). Advection of water vapor toward Hawai'i by the upper low begins soon after this time, transporting moisture from the convective eastern side around to the north of the low-pressure center [*Caruso and Businger*, 2006]. LAPS PW analysis indicates the presence of an advective "tongue" extending north and west of the low-pressure center, which consists of a boundary between an area of high PW and an area of lower PW in front of it (Figure 6a). The outer boundary of this PW "tongue" reaches the ship's location, northeast of the Island of Hawai'i, at 1400 HST on

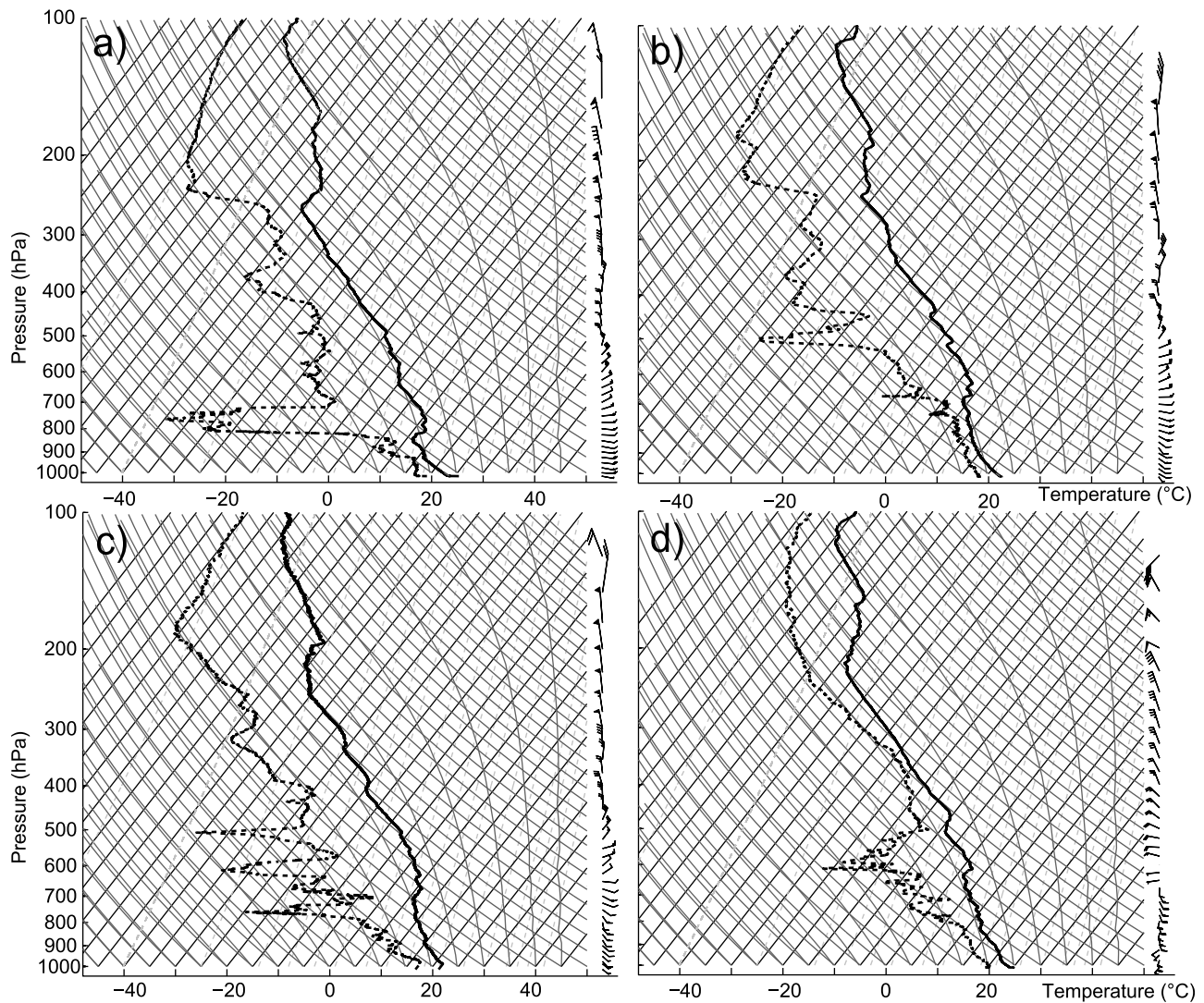


**Figure 5.** Radiosonde profiles of  $T$  (solid line) and  $T_d$  (dashed line) for (a) Radiosonde No. 9 (1948 HST on 2 February), (b) Radiosonde No. 12 (0515 HST on 4 February), (c) Radiosonde No. 13 (1414 HST on 4 February), and (d) Radiosonde No. 21 (1533 HST on 6 February).

3 February (Figure 2). At this time, an associated transition is apparent in the GPS PW time series, increasing by 15 mm in  $\sim 19$  h. Upper air soundings from radiosondes No. 9–12 were taken as the PW tongue crossed the ship's location. Sounding No. 9 (Figure 5a) shows a large dry slot at 700–800 mb associated with a trade wind inversion and as the PW tongue moves over the ship, the trade wind inversion begins to decay. By sounding No. 12 (Figure 5b), the air mass above the ship is clearly quite different. Most of the moisture is located below 700 mb, with a now stronger dry slot at 500 mb. Vertical-velocity values derived from the radiosonde profiles also show an increase from  $\sim 2.5$   $\text{ms}^{-1}$  to  $\sim 4$   $\text{ms}^{-1}$  on average throughout the troposphere between radiosondes No. 9 and No. 12 [Wang *et al.*, 2009].

[21] The steady rise in GPS PW, due to moisture advected by the PW tongue, continues until 0700 HST on 4 February, at which point the increase ceases and a steep drop off begins (Figure 2). GPS PW decreases steeply from this time until a local minimum of 23.6 mm is reached at 1400 HST on 4 February, matching values seen on 2 February before

the upper low began to affect the islands. Radiosonde 13 was launched at the time of this minimum (Figure 5c) and the resulting sounding reveals several dry slots in the mid troposphere between 450 and 800 mb, indicating an absence of the PW tongue seen in Figure 6a. The upper low continues its track southward past Hawai'i on the morning of 4 February (Figure 7) and the high PW area associated with it also moves south, causing the boundary of the tongue to again pass over the ship and cause the steep drop in PW.

[22] At 1400 HST on 4 February, LAPS PW analysis (Figure 6b) identified a large area of high PW to the southeast of Hawai'i, which is associated with the upper low. The anemometer aboard the KM detected a gradual shift in the large-scale low-level winds from normal trade winds to southeasterly flow on the morning of 4 February, associated with a cold front approaching from the northwest. This wind shift causes advection of low-level moisture from the area southeast of the islands toward the northwest, and the ship again experiences a PW tongue. As a result, GPS PW begins to rise steeply again. This occurs between 1400 HST on 4

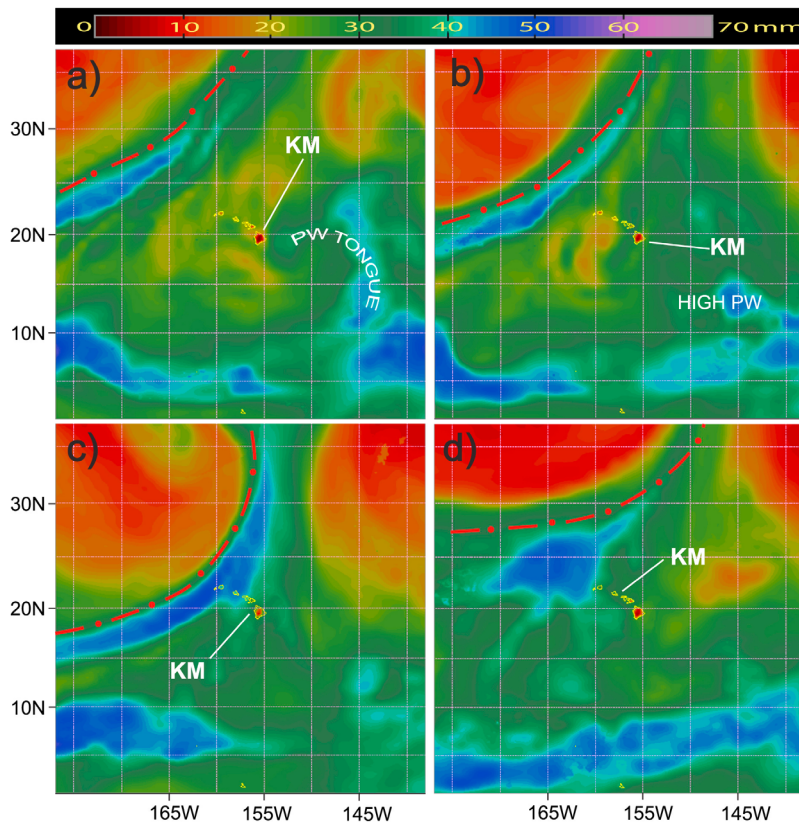


**Figure 6.** LAPS PW output for (a) 1400 HST 3 February with high PW tongue, (b) 1400 HST on 4 February with high PW area to the SE of the Islands, (c) 1400 HST on 6 February showing the first shear line (broken red line), and (d) 0800 HST on 9 February showing the second shear line. KM denotes the position of the *Kilo Moana*.

February and 0000 HST on 5 February, at which point the GPS PW reaches values matching those seen at 0700 HST on 4 February (Figure 2). By 6 February, GOES WV imagery (not shown) shows that the upper low has tracked eastward, and then northeastward, as is typical for the dissipating stage [Caruso and Businger, 2006].

[23] LAPS analyses at 0800 HST on 6 February shows a band of increased surface wind speed (Figure 8a) and 600 mb relative humidity (Figure 8b) at Kaua’i’s northwestern coast, with no apparent temperature gradient at 600mb (Figure 8c) or change in surface wind direction (Figure 8a), suggesting that a shear line has reached the islands. The cloud patterns in Figure 9 show the evolution of the cloud band associated with the shear line as it moves in from the northwest, bringing with it a band of high PW (Figure 6c). On the morning of 6 February, the KM began its journey from the Kona coast of the Island of Hawai’i toward the north shores of Maui and Moloka’i via the Alenuihaha Channel (Figure 1). As it moves northward, a broad maximum of GPS PW is seen over the ship, with the maximum PW for the field experiment peaking at 1615 HST on 7 February (Figure 2).

[24] The moisture increase over the ship due to the shear line is greatest in the upper levels, as suggested by the sounding from radiosonde No. 21, taken at 1533 HST on 6 February when the KM was located off the Island of Hawai’i’s Kona coast (Figure 5d). Radar also identifies

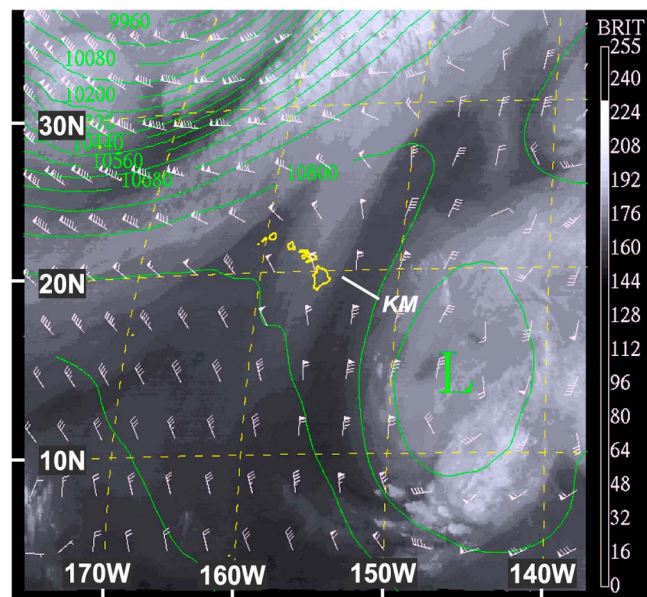


**Figure 7.** GOES WV images with Global Forecast Model (GFS) 250 mb height and wind analysis overlays for 0800 HST 4 February, showing the upper low moving south and away from the islands. KM indicates the position of the *Kilo Moana*.

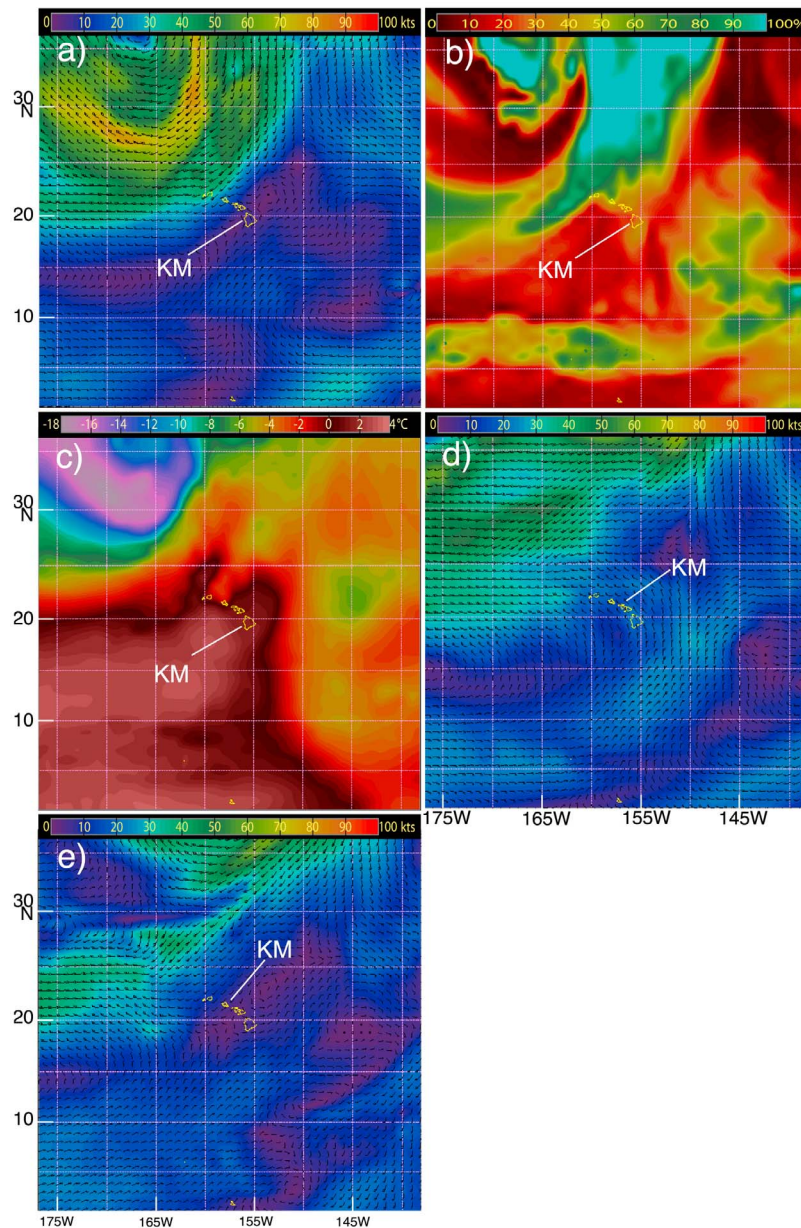


**Figure 8.** LAPS analysis for (a) surface wind speed and direction at 0800 HST on 6 February, (b) 600 mb relative humidity at 0800 HST on 6 February, (c) 600 mb temperature at 0800 HST on 6 February, (d) surface wind speed and direction at 0800 HST on 7 February, and (e) surface wind speed and direction at 0800 HST on 9 February. KM denotes the position of the *Kilo Moana*.

strong echoes moving over the islands in the upper levels from the northwest, with the majority of the echoes not extending further south than the islands of Kaua'i, O'ahu, and Moloka'i (not shown). By 0800 HST on 7 February, LAPS surface winds no longer show any wind speed gradient near the islands, suggesting that the shear line has dissipated (Figure 8d). However, associated moisture still lingers in the LAPS PW field at this time, creating a lag between the beginning of the shear line's dissipation and the GPS PW maximum at 1615 HST on 7 February.

[25] The PW pattern observed toward the end of the data period is dominated by a second shear line, identifiable by an area of increased wind speeds northwest of Kaua'i in the

LAPS surface winds at 0800 HST on 9 February (Figure 8e). This shear line is substantially weaker than the first, and the wind speed gradient does not quite reach the islands. However, associated moisture does reach the islands (Figure 6d), causing a change from decreasing to increasing GPS PW values at this time (Figure 2). This steady GPS PW increase concludes the data collection period, with this band of higher PW arriving at the Kaua'i west coast as the ship makes for Honolulu.

### 3.2. Island Scale Features

[26] At the beginning of the field experiment, the islands experienced PW values below those typically seen in

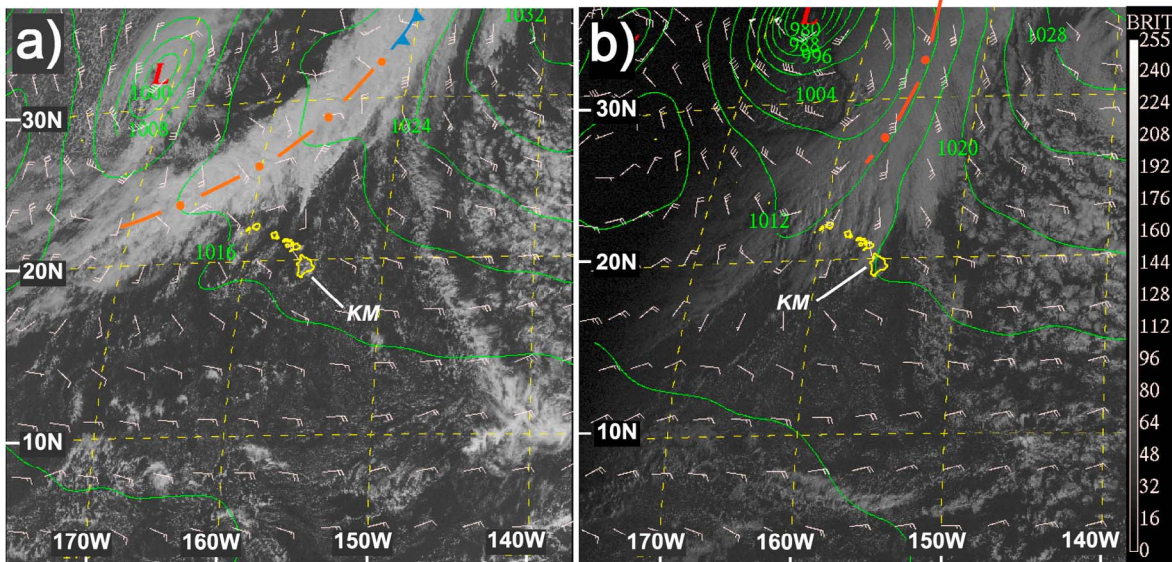


**Figure 9.** (a) GOES VIS images with Global Forecast Model (GFS) surface pressure and wind analysis overlays for 1100 HST on 5 February showing the first shear line (broken red line) and (b) 0800 HST on 6 February, showing the first shear line as it reaches the islands. The position of the *Kilo Moana* (KM) is indicated.

Hawai'i [Motell *et al.*, 2002]. On leaving Honolulu on the morning of 1 February, the KM circled O'ahu's eastern tip and traveled to the windward coast (Figure 1). Figure 2 shows a spike in GPS PW at 1930 HST on 1 February, where possible orographic blocking by O'ahu's terrain causes moisture to build on the windward side of the island [Chen and Nash, 1994]. The temporal positioning of this spike agrees well with the position of the ship relative to the island, and GPS PW decreases as the ship moves southward through the Kaiwi Channel and past the leeward areas of Maui and Lana'i (Figures 1 and 3). After navigating the Alenuihaha Channel, the effects from the upper low-pressure system described in the previous section begin to dominate the GPS time series.

[27] The ship traveled toward the Island of Hawai'i on 4 February from the northeast, and approached the Kilauea coast the next morning (Figure 10). This island typically produces more island-induced effects on weather than any of the others, due to its large size and altitude [Smith and Grubišić, 1993; Chen and Nash, 1994; Carbone *et al.*, 1998]. The patterns in wind direction and GPS PW shown in Figures 10 and 3 are related and may be explained by a feature referred to by Carbone *et al.* [1998] as the "flow separation line" (FSL) and by Li and Chen [1999] as the "drainage front." The thermally induced westerly downslope flow at Hilo meets the incoming trade wind flow under normal trade wind conditions, creating a line of low-level convergence. Li and Chen [1999] identify three types of related rainbands throughout the day, one of which occurs in the early morning around sunrise, and both Carbone *et al.* [1998] and Li and Chen [1999] identify an area of convergence that extends ~20 km offshore at this time of day. This area of convergence has an associated cloud band shown by MODIS RGB (Figure 11). From 0245 HST until 0800 HST on 5 February, the KM tracked close (~4 km) to the Kilauea coast, before moving offshore again (~25 km). The timing

of this track into the convergence zone closely matches a peak observed in GPS PW marked in Figure 2. There are likely to be minor differences in the timing and positioning of the convergence line for this case because the flow is southeasterly on this day, however, the general structure is present, as can be inferred from the ship surface wind observations (Figure 10).

[28] Another peak in GPS PW occurred at 2100 HST on 5 February (Figure 12). This peak results from the ship's passage through a small convergence zone at the southern tip of the Island of Hawai'i (Figure 11). As the southeasterly low-level flow encounters the island, high pressure builds. Air is then forced around the southern tip, converging with

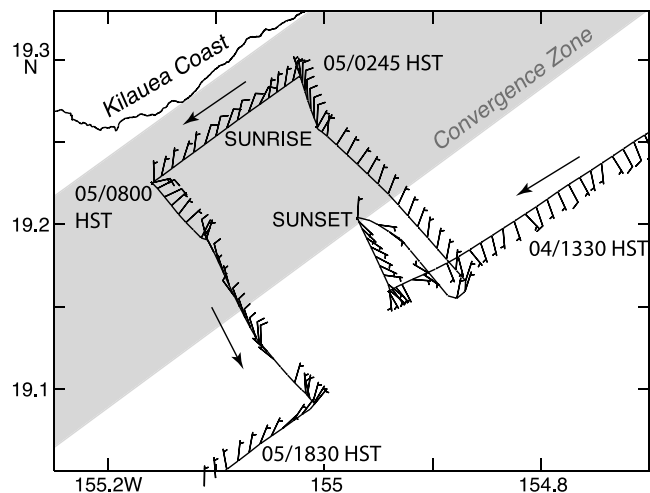


**Figure 10.** *Kilo Moana* track with windbarbs as the ship passes the Kilauea Coast (4–5 February). The ship enters a convergence zone here causing a peak in GPS PW between 0245 HST and 0800 HST on 5 February.

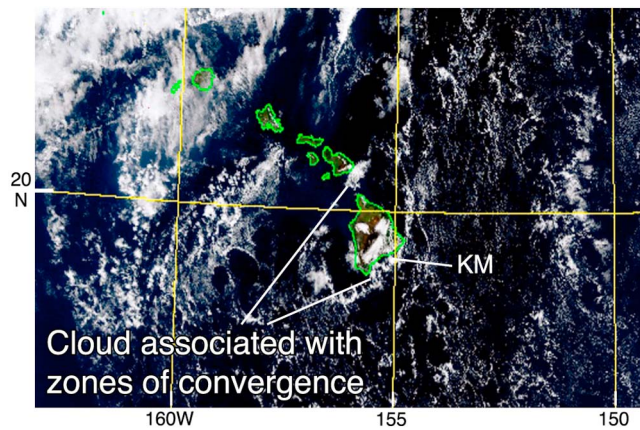


**Figure 11.** MODIS RGB visible composite for 1050 HST on 5 February. The cloud bands to the southeast of the Island of Hawai‘i and the southeast of Maui imply the presence of convergence zones in these areas.

the large-scale southeasterly flow to the south. The passage of the ship through this convergence zone matches the timing of the associated peak labeled in Figure 2.

[29] The maximum PW value estimated by GPS during the field experiment before smoothing is 45 mm, and occurs at the apex of a sharp peak in PW at 2215 HST on 6 February (Figure 2). The spike is the result of the ship sailing through a convergence zone created by the wake of the Island of Hawai‘i under the southeast flow; Figure 13 shows wind convergence off the southeastern coast of Maui, where air flowing from the northern and southern sides of the Island of Hawai‘i meet. Although the spike in PW occurs at night, when no cloud information is available, a cloud band formed by a similar convergence zone can be seen in Figure 11 for the previous day. The ship enters this area at 2100 HST on 6 February, when the GPS PW begins to rise. The peak occurs at 2215 HST, as the ship travels southeast for a brief

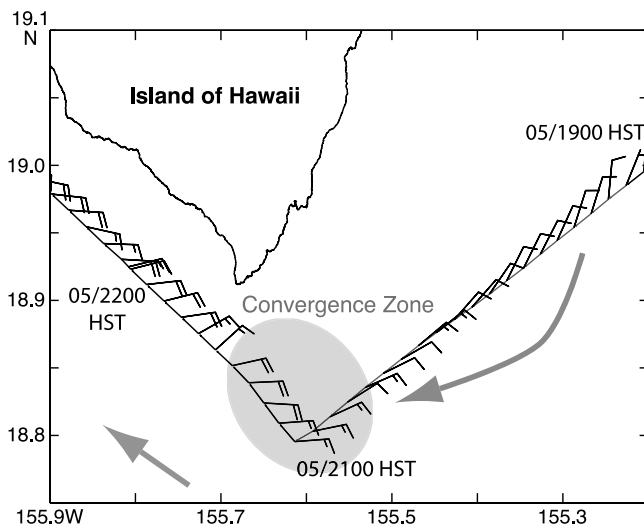


**Figure 12.** *Kilo Moana* track with windbarbs as the ship passes the southern tip of the Island of Hawai‘i. A convergence zone is formed (shaded area) as the air flowing around the island meets the large-scale flow.

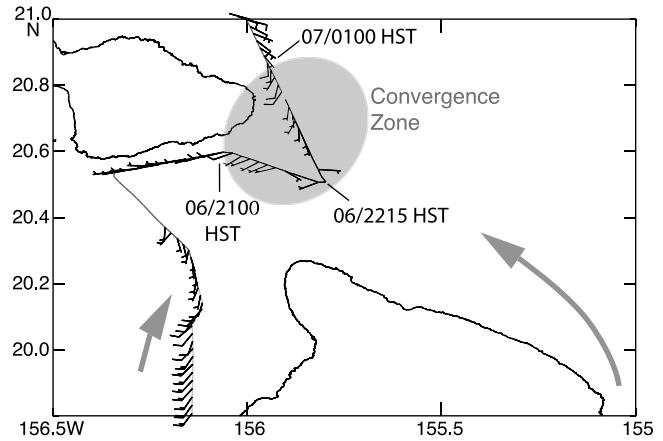


**Figure 13.** *Kilo Moana* track and wind barbs for the evening of 6 February. A convergence zone created by the wake of the Island of Hawai‘i is present (shaded area). GPS PW spikes as the ship passes through this convergence zone.

interval. Afterwards, the ship moves northwest toward the Maui windward coast. The GPS PW spike ends as the ship leaves the convergence zone at 0100 HST on 7 February. Note that a wind shift is observed by the KM anemometer at this time from southwesterly to southeasterly flow as the influence of the island and channel flows comes to an end, along with the low-level convergence associated with them (Figure 13).

#### 4. Summary and Conclusions

[30] A time series of precipitable water-vapor estimates from the GPS receivers aboard the research vessel *Kilo Moana* was created and validated for a cruise around the Hawaiian coastal waters. The field experiment lasted ten days and experienced a variety of weather that encompassed both synoptic and mesoscale features. The PW time series was found to agree with radiosonde PW observations taken throughout the cruise. The RMS difference in PW between GPS and radiosonde is found to be 2.16 mm. Although this value is slightly higher than that found by *Rocken et al.* [2005], the atmosphere was probably more dynamically unstable and heterogeneous than for the case described by *Rocken et al.* [2005]. This RMS value is nonetheless comparable to land based PW estimates [*Businger et al.*, 1996; *Motell et al.*, 2002].

[31] The GPS PW estimates were able to identify the water-vapor signatures of three main synoptic scale features—an upper level low-pressure system and two shear lines, which were responsible for the signals with the greatest magnitude during the field experiment. In addition, the data set was able to identify various island-induced features in the time series, many of which were related to zones of horizontal convergence. The passage of the ship through these zones matched the timing of the peaks observed in the time series.

[32] The technique is also able to resolve the time evolution of atmospheric features. The moisture distribution associated with the first shear line, which reached the islands on 6 February, evolved in the GPS PW time series as it moved across the western side of the island chain. The PW

signature of the upper-low pressure system also evolved throughout the early part of the time series. The added temporal resolution of the PW data makes the time series particularly useful in analyzing the time evolution of such features.

## 5. Discussion

[33] The technique described here may be superior to traditional methods of ocean PW estimation using radiosonde or satellite data. Radiosonde PW observations have very limited temporal resolution, and are restricted by the balloon's horizontal trajectory, which follows the winds, while GPS PW represents the vertical column above the receiver, based on an average over the volume around the antenna described by the raypaths from all tracked satellites. GPS PW is also available through cloud/rain and at night, unlike the case of satellite-based PW estimation.

[34] Analysis of mesoscale weather was not the primary scientific focus of this field experiment. Future research could choose ship tracks that concentrate on documenting water vapor distributions associated with island-scale influences. The islands' diurnally driven rainbands, convergence lines, and other effects could hopefully then be understood to a greater degree [Carbone *et al.*, 1998; Li and Chen, 1999]. If such a field experiment were undertaken with multiple vessels in proximity, the spatial resolution could also be enhanced for any given epoch.

[35] The availability of GPS estimates over the oceans could provide a powerful constraint to NWP models. A suggested future outcome of these findings could be the development of a large network of ocean-based PW estimates from merchant and military vessels. Wintertime synoptic scale systems, which produce broad cloud and precipitation shields, limit satellite estimation of PW. Therefore, a network like this could improve the accuracy of operational forecasting of winter storms over the ocean and in coastal areas [e.g., Gutman *et al.* 2004]. Ocean-based PW data could also assist operational weather centers in analyzing tropical cyclones and kona (subtropical) storms, which tend to have erratic tracks and are a challenge to model and forecast [Morrison and Businger, 2001].

[36] All the reference sites used in the PW processing in this paper are also processed in an hourly near-real-time GPS meteorology network, so good a-priori ZND estimates are available within  $\sim 1$  h. Reasonable predictions based on the previous few hours solutions could be available in real-time. To produce near-real-time estimates from a ship would require either a real-time data stream and real-time kinematic processing, or half-hourly/hourly data downloads and post-processed kinematic solutions. In either case ZND estimates for the ship could also be available within an about an hour of the most recent data. If we wait until the best ZND estimates are available for the reference sites, accurate ship-board PW estimates could be comfortably generated within two hours of the latest acquired data.

[37] Although we use IGS final orbits for our processing, we can estimate the impact of adopting an operational real-time protocol and using the IGS combined ultra-rapid orbits, which include a 24-h prediction. The current accuracy of the predicted half of the ultra-rapid orbits is estimated as  $\sim 5$  cm (<http://igsceb.jpl.nasa.gov/components/prods.html>, accessed

22 Apr 2012). This introduces  $<1$  mm ZND, or  $<0.15$  mm PW bias [e.g., Ge *et al.*, 2002; Tregoning *et al.*, 1998] with respect to the  $\sim 2.5$  cm accuracy final orbits. Although the accuracy can be expected to drop dramatically toward the end of the 24-h predictions, with updated ultra-rapid solutions available every 6 h we would expect real-time solutions using the IGS ultra-rapid products to have  $<0.2$  mm additional PWV error.

[38] In summary, the high temporal resolution of the technique described in this paper, combined with the ability of the receiver to move spatially, makes this new data set ideal for the investigation of water vapor on small scales. Water vapor is highly inhomogeneous and accurate knowledge of its distribution has been difficult to obtain over the ocean in the past. Equipping some portion of the commercial and military fleets to provide near real time data for GPS meteorology would increase the availability of PW estimates, which could then be used as an aid to better understand the dynamics of this important variable in the oceanic environment.

[39] **Acknowledgments.** We would like to thank David Hitzl for providing the radiosonde data used in this study and Nancy Hultiz for assistance with the figures. We are also grateful to John J. Braun and two anonymous reviewers for their thoughtful reviews, which contributed to a better paper. This research was supported by NSF grants EAR-0746394 and OCE-0906811.

## References

- Bevis, M., S. Businger, T. A. Herring, C. Rocken, R. A. Anthes, and R. H. Ware (1992), GPS meteorology: Remote sensing of atmospheric water vapor using the global positioning system, *J. Geophys. Res.*, *97*, 15,787–15,801, doi:10.1029/92JD01517.
- Bevis, M., S. Businger, S. Chiswell, T. A. Herring, R. Anthes, C. Rocken, and R. H. Ware (1994), GPS meteorology: Mapping zenith wet delays onto precipitable water, *J. Appl. Meteorol.*, *33*, 379–386, doi:10.1175/1520-0450(1994)033<0379:GMMZWD>2.0.CO;2.
- Businger, S., S. Chiswell, M. Bevis, J. Duan, R. Anthes, C. Rocken, R. Ware, T. Van Hove, and F. Solheim (1996), The promise of GPS in atmospheric monitoring, *Bull. Am. Meteorol. Soc.*, *77*, 5–18, doi:10.1175/1520-0477(1996)077<0005:TPOGIA>2.0.CO;2.
- Carbone, R., J. D. Tuttle, W. A. Cooper, V. Grubisic, and W.-C. Lee (1998), Tradewind rainfall near the windward coast of Hawai'i, *Mon. Weather Rev.*, *126*, 2847–2863, doi:10.1175/1520-0493(1998)126<2847:TWRNTW>2.0.CO;2.
- Caruso, S. J., and S. Businger (2006), Subtropical cyclogenesis over the central North Pacific, *Weather Forecast.*, *21*, 193–205, doi:10.1175/WAF914.1.
- Chadwell, C. D., and Y. Bock (2001), Direct estimation of absolute precipitable water in oceanic regions by GPS tracking of a coastal buoy, *Geophys. Res. Lett.*, *28*, 3701–3704, doi:10.1029/2001GL013280.
- Chen, Y.-L., and A. J. Nash (1994), Diurnal variation of surface airflow and rainfall frequencies on the Island of Hawai'i, *Mon. Weather Rev.*, *122*, 34–56, doi:10.1175/1520-0493(1994)122<0034:DVOSAA>2.0.CO;2.
- Cherubini, T., S. Businger, C. Velden, and R. Ogasawara (2006), The impact of satellite-derived atmospheric motion vectors on mesoscale forecasts over Hawai'i, *Mon. Weather Rev.*, *134*(7), 2009–2020, doi:10.1175/MWR3163.1.
- Duan, J., *et al.* (1996), GPS meteorology: Direct estimation of the absolute value of precipitable water, *J. Appl. Meteorol.*, *35*, 830–838, doi:10.1175/1520-0450(1996)035<0830:GMDEOT>2.0.CO;2.
- Foster, J., M. Bevis, S. Businger, Y.-L. Chen, and Y. Zhang (2003), The Ka'u storm (November 2000), Imaging precipitable water using GPS, *J. Geophys. Res.*, *108*(D18), 4585, doi:10.1029/2003JD003413.
- Foster, J., M. Bevis, and S. Businger (2005), GPS meteorology: Sliding-window analysis, *J. Atmos. Oceanic Technol.*, *22*, 687–695, doi:10.1175/JTECH1717.1.
- Foster, J. H., B. A. Brooks, D. Wang, G. S. Carter, and M. A. Merrifield (2012), Improving tsunami warning using commercial ships, *Geophys. Res. Lett.*, *39*, L09603, doi:10.1029/2012GL051367.
- Gao, B.-C., and Y. J. Kaufman (2003), Water vapor retrievals using Moderate Resolution Imaging Spectroradiometer (MODIS) near-infrared channels, *J. Geophys. Res.*, *108*(D13), 4389, doi:10.1029/2002JD003023.

- Ge, M., E. Calais, and J. Haase (2002), Sensitivity of zenith total delay accuracy to GPS orbit errors and implications for near-real-time GPS meteorology, *J. Geophys. Res.*, *107*(D16), 4315, doi:10.1029/2001JD001095.
- Gradinarsky, L. P., J. M. Johansson, H. R. Bouma, H.-G. Scherneck, and G. Elgered (2002), Climate monitoring using GPS, *Phys. Chem. Earth*, *27*, 335–340, doi:10.1016/S1474-7065(02)00009-8.
- Gutman, S. I., S. R. Sahn, S. G. Benjamin, B. E. Schwartz, K. L. Holub, J. Q. Stewart, and T. L. Smith (2004), Rapid retrieval and assimilation of ground based GPS precipitable water observations at the NOAA forecast systems laboratory: Impact on weather forecasts, *J. Meteorol. Soc. Jpn.*, *82*, 351–360, doi:10.2151/jmsj.2004.351.
- Herring, T. A. (2006), TRACK version 1.13 GPS kinematic positioning program, Mass. Inst. of Technol., Cambridge.
- Hiemstra, C. A., G. E. Liston, R. A. Pielke Sr., D. L. Birkenheuer, and S. C. Albers (2006), Comparing local analysis and prediction system (LAPS) assimilations with independent observations, *Weather Forecast.*, *21*, 1024–1040, doi:10.1175/WAF961.1.
- Kuo, Y.-H., Y.-R. Guo, and E. Westwater (1993), Assimilation of precipitable water measurements into a mesoscale numerical model, *Mon. Weather Rev.*, *121*, 1215–1238, doi:10.1175/1520-0493(1993)121<1215:AOPWMI>2.0.CO;2.
- Li, J., and Y.-L. Chen (1999), A case study of nocturnal rainshowers over the windward coastal region of the island of Hawai'i, *Mon. Weather Rev.*, *127*, 2674–2692, doi:10.1175/1520-0493(1999)127<2674:ACSONR>2.0.CO;2.
- Li, Z. H., J. P. Muller, and P. Cross (2003), Tropospheric correction techniques in repeat-pass SAR interferometry, paper presented at FRINGE 200, Eur. Space Res. Inst., Frascati, Italy.
- Miloshevich, L. M., H. Vömel, D. N. Whiteman, B. M. Lesht, F. J. Schmidlin, and F. Russo (2006), Absolute accuracy of water vapor measurements from six operational radiosonde types launched during AWEX-G and implications for AIRS validation, *J. Geophys. Res.*, *111*, D09S10, doi:10.1029/2005JD006083.
- Morrison, I., and S. Businger (2001), Synoptic structure and evolution of a Kona low, *Weather Forecast.*, *16*, 81–98, doi:10.1175/1520-0434(2001)016<0081:SSAEOA>2.0.CO;2.
- Motell, C., J. Porter, J. Foster, M. Bevis, and S. Businger (2002), Comparison of precipitable water over Hawai'i using AVHRR-based split-window techniques, GPS and radiosondes, *Int. J. Remote Sens.*, *23*(11), 2335–2339, doi:10.1080/01431160110069944.
- Porter, J. N., B. R. Lienert, S. K. Sharma, E. Lau, and K. Horton (2003), Vertical and horizontal aerosol scattering fields over Bellows Beach, Oahu, during the SEAS experiment, *J. Atmos. Oceanic Technol.*, *20*(10), 1375–1387, doi:10.1175/1520-0426(2003)020<1375:VAHASF>2.0.CO;2.
- Rocken, C., R. Ware, R. VanHove, T. Solheim, F. Alber, C. Johnson, J. M. Bevis, and S. Businger (1993), Sensing atmospheric water vapor with the global positioning system, *Geophys. Res. Lett.*, *20*, 2631–2634, doi:10.1029/93GL02935.
- Rocken, C., T. Van Hove, T. Johnson, F. Solheim, R. H. Ware, M. Bevis, S. Businger, and S. R. Chiswell (1995), GPS/STORM-GPS sensing of atmospheric water vapor for meteorology, *J. Atmos. Oceanic Technol.*, *12*, 468–478, doi:10.1175/1520-0426(1995)012<0468:GSOAWV>2.0.CO;2.
- Rocken, C., T. Van Hove, and R. Ware (1997), Near real-time sensing of atmospheric water vapor, *Geophys. Res. Lett.*, *24*, 3221–3224, doi:10.1029/97GL03312.
- Rocken, C., J. Johnson, T. Van Hove, and T. Iwabuchi (2005), Atmospheric water vapor and geoid measurements in the open ocean with GPS, *Geophys. Res. Lett.*, *32*, L12813, doi:10.1029/2005GL022573.
- Simpson, R. H. (1952), Evolution of the Kona storm, a subtropical cyclone, *J. Meteorol.*, *9*, 24–35, doi:10.1175/1520-0469(1952)009<0024:EOTKSA>2.0.CO;2.
- Smith, R. B., and V. Grubišić (1993), Aerial observations of Hawai'i's wake, *J. Atmos. Sci.*, *50*, 3728–3750, doi:10.1175/1520-0469(1993)050<3728:AOOHV>2.0.CO;2.
- Smith, T. L., S. G. Benjamin, S. I. Gutman, and S. R. Sahn (2007), Short-range forecast impact from assimilation of GPS-IPW observations into the rapid update cycle, *Mon. Weather Rev.*, *135*, 2914–2930, doi:10.1175/MWR3436.1.
- Sohn, B.-J., and E. A. Smith (2003), Explaining sources of discrepancy in SSM/I water vapor algorithms, *J. Clim.*, *16*(20), 3229–3255, doi:10.1175/1520-0442(2003)016<3229:ESODII>2.0.CO;2.
- Tregoning, P., R. Boers, D. O'Brien, and M. Hendy (1998), Accuracy of absolute precipitable water vapor estimates from GPS observations, *J. Geophys. Res.*, *103*, 28,701–28,710.
- Wang, J., J. Bian, W. O. Brown, H. Cole, V. Grubišić, and K. Young (2009), Vertical air motion from T-REX radiosonde and dropsonde data, *J. Atmos. Oceanic Technol.*, *26*(5), 928–942, doi:10.1175/2008JTECHA1240.1.